ACS NANO

www.acsnano.org

ARTICLE

Monitoring $Ti_3C_2T_x$ MXene Degradation Pathways Using Raman Spectroscopy

Sonata Adomaviciute-Grabusove,* Anton Popov, Simonas Ramanavicius,* Valdas Sablinskas, Kateryna Shevchuk, Oleksiy Gogotsi, Ivan Baginskiy, Yury Gogotsi, and Arunas Ramanavicius*

Cite This: *ACS Nano* 2024, 18, 13184–13195

Read Online

ACCESS | Metrics & More | Article Recommendations | Supporting Information

ABSTRACT: **Extending applications of $Ti_3C_2T_x$ MXene in nanocomposites and across fields of electronics, energy storage, energy conversion, and sensor technologies necessitates simple and efficient analytical methods. Raman spectroscopy is a critical tool for assessing MXene composites; however, high laser powers and temperatures can lead to the materials' deterioration during the analysis. Therefore, an in-depth understanding of MXene photothermal degradation and changes in its oxidation state is required, but no systematic studies have been reported. The primary aim of this study was to investigate the degradation of the MXene lattice through Raman spectroscopic analysis. Distinct spectral markers were related to structural alterations within the $Ti_3C_2T_x$ material after subjecting it to thermal- and laser-induced degradation. During the degradation processes, spectral markers were revealed for several specific steps: a decrease in the number of interlayer water molecules, a decrease in the number of −OH groups, formation of C−C bonds, oxidation of the lattice, and formation of TiO_2 nanoparticles (first anatase, followed by rutile). By tracking of position shifts and intensity changes for $Ti_3C_2T_x$, the spectral markers that signify the initiation of each step were found. This spectroscopic approach enhances our understanding of the degradation pathways of MXene, and facilitating enhanced and dependable integration of these materials into devices for diverse applications, from energy storage to sensors.**

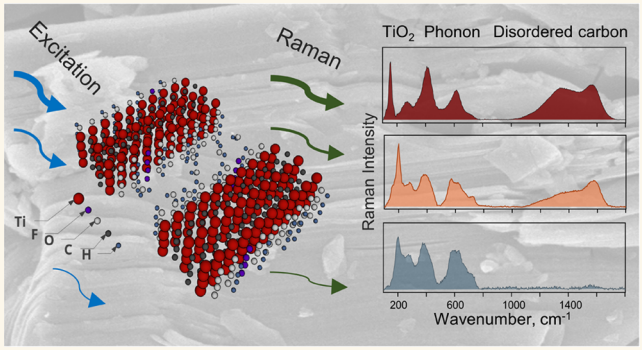

KEYWORDS: *2D materials, MXenes, Raman spectroscopy, TiO_2 nanoparticles, $Ti_3C_2T_x$, MXene degradation, laser-induced disruption*

INTRODUCTION

The rapidly expanding family of two-dimensional (2D) materials, MXenes, emerged with the discovery of 2D $Ti_3C_2T_x$ in 2011.[1,2] MXenes are carbides, nitrides, oxycarbides, and carbonitrides of transition metals with the general formula $M_{n+1}X_nT_x$ (where n = 1, 2, 3, or 4; M depicts a transition metal, *e.g.*, Ti, V, Nb, Mo; X represents C and/or N (O substitution is possible); T_x refers to surface functional groups, *e.g.*, −OH, −F, = O, *etc.*). MXenes are generally produced by selectively etching the middle element A of the parent MAX phase (where A refers to elements from the main groups III−VI, such as Al or Si), thus releasing 2D MX layers. Multiple layers of MXenes are further separated by various intercalants and/or sonication, yielding 2D MXenes. In particular, $Ti_3C_2T_x$ MXene has a long history of research and is notable for inexpensive synthesis from earth-abundant elements and its outstanding properties, such as high conductivity, hydrophilicity, redox-active surfaces, *etc.*[3−5] Further investigations are also directed toward efficiently producing different MXene types that can yield defect-free 2D MXene layers.[4,6]

The increasing attention to MXene can be attributed, in part, to its wide range of applications across various fields, including energy storage[5,7−9] and conversion[3,9,10] (such as supercapacitors and batteries), sensor development,[11−19] electronic components,[7,8,20−23] and the fabrication of nanocomposites for numerous other applications.[5] Many optical,[24] electronic,[9] and chemical properties[25] of MXene depend on structural changes, including variations in material oxidation state,[9,22,24,26] and the presence of amorphous carbon or TiO_2 nanoparticles[27−29] that arise during lattice degradation.[30−33] The sensitivity of MXene to environmental and structural changes makes it an excellent sensor material. MXene can function as a sensor on its own[11−15] or be integrated as a

Received: February 14, 2024
Revised: April 16, 2024
Accepted: April 25, 2024
Published: May 6, 2024

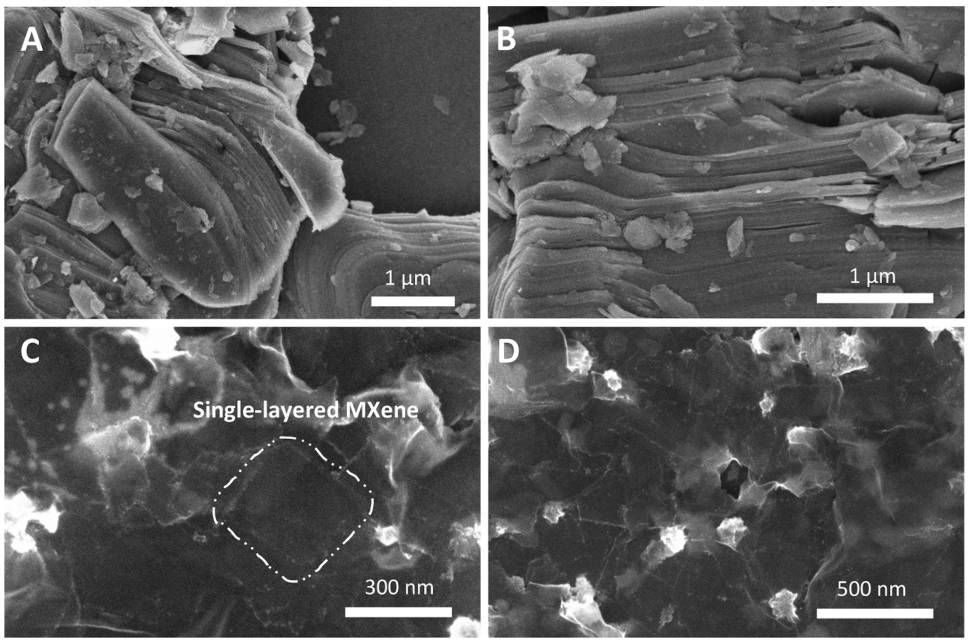

Figure 1. SEM images of multilayered powder (A, B) and delaminated single-layered films of (C, D) $Ti_3C_2T_x$ MXene.

crucial component in nanocomposites for sensor applications.[13,16−19]

Raman spectroscopy is a powerful analytical technique used to study the stability and degradation properties of materials,[34−40] and it is particularly useful for assessing MXene quality during fabrication of devices and sensors. It is sensitive to interactions between chemical species and alterations in lattice structures, making it applicable to detect the presence of amorphous compounds, as well as traces of transition metal oxides commonly found in the structure of MXene. The Raman spectra can reveal detailed information about the structural and surface chemistry of MXenes,[41] detect TiO_2 structures,[42−44] and assess lattice oxidation and degradation,[22,24,45,46] among other valuable applications.[24,42,43,47] Raman spectroscopy-guided sensor development provides enhanced performance, while Raman assessment ensures quality during composite fabrication. Moreover, the application of MXene in sensor technology not only benefits from Raman spectroscopy for analysis but also contributes to the advancement of Raman spectroscopy techniques, enhancing their sensitivity and broadening their applicability.[7,8,20,24,48]

The Raman spectral bands of $Ti_3C_2T_x$ MXene have been assigned to lattice phonon modes based on density functional theory calculations and additional computational methods.[41,42,49] Notably, while most computational predictions were based on homogeneous surface groups (=O, −OH, and −F), MXene terminations appear to be inhomogeneous when synthesized by the wet chemical etching method. The presence of complex surface groups has been confirmed by computational calculations[50−53] in tandem with analytical techniques,[54,55] *e.g.*, pair distribution function (PDF), X-ray photoelectron spectroscopy (XPS), electron energy loss spectroscopy (EELS), and Raman spectroscopy.[24,43,49,51,55] Due to the mixed terminations and defects in the MXene lattice, the deconvolution of Raman spectra can be very complicated. Nevertheless, a recent study utilized machine-learning force field computations to provide further insights into the nature of complex Raman bands by incorporating computational Raman modes for hybrid surface groups along with the concept of symmetry breaking in the lattice.[51] This approach successfully explained the broadening of Raman bands and the appearance of additional in-plane modes when considering hybrid −O(OH) surface groups.

The primary objective of this study is to uncover the spectral changes observed in treated MXene films. It includes tentative assignments of these features to the vibrational modes discussed in the literature.[24,43,49,51] However, it should be emphasized that the observed changes in the Raman spectra are not exclusive to any specific termination type. Instead, they are a result of the overall structural complexity arising from the presence of various terminations in the MXene samples. This study also highlights the effects of film degradation on MXene Raman spectra, which encompass oxygenation and deterioration of the MXene lattice, reduction of interlayer water, and other changes.[9,56−59] In particular, we focused on the Raman spectral markers associated with processes resulting from laser-induced changes, such as oxidation and partial destruction of the lattice. Further investigations of lattice transitions were conducted by using the thermal treatment of MXene films. In general, spectral differences in the Raman spectra of the degraded MXene films were found, which can be attributed to (I) a decrease in the number of molecules trapped between the MXene sheets, (II) the decrease in the number of −OH groups, and (III) oxidation of MXene. Understanding MXene degradation pathways may contribute to the design of energy storage and sensor materials with improved stability. Therefore, the findings presented in this study guide sensor development, enabling precise detection in diverse applications.

RESULTS

Scanning Electron Microscopy (SEM), Energy-Dispersive X-ray (EDX) Analysis, X-ray Diffraction (XRD), and Visible−Near-Infrared (Vis−NIR) Spectroscopy Characterization of Synthesized MXene. The morphology

https://doi.org/10.1021/acsnano.4c02150
ACS Nano 2024, 18, 13184−13195

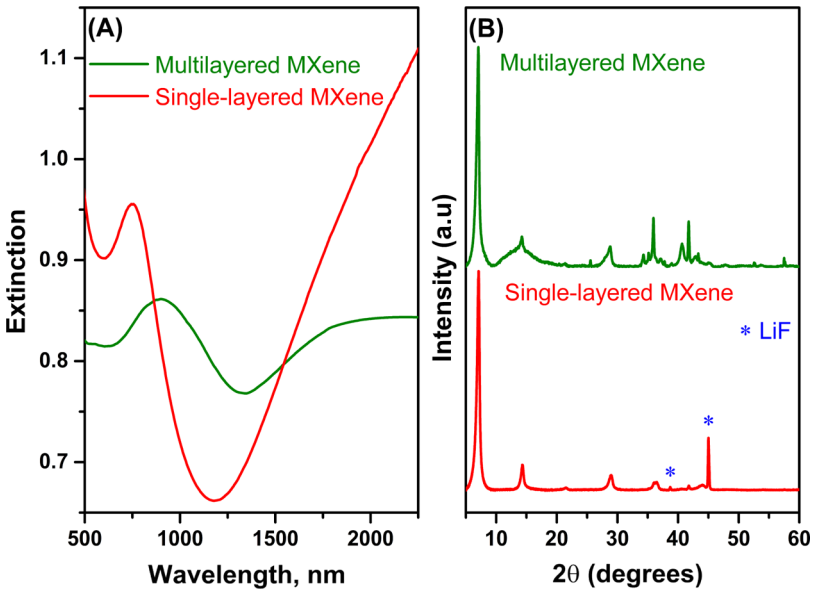

Figure 2. Comparison between the multilayered and single-layered MXene samples. (A) Vis−NIR absorption spectrum and (B) XRD patterns of multilayered and delaminated single-layered MXene.

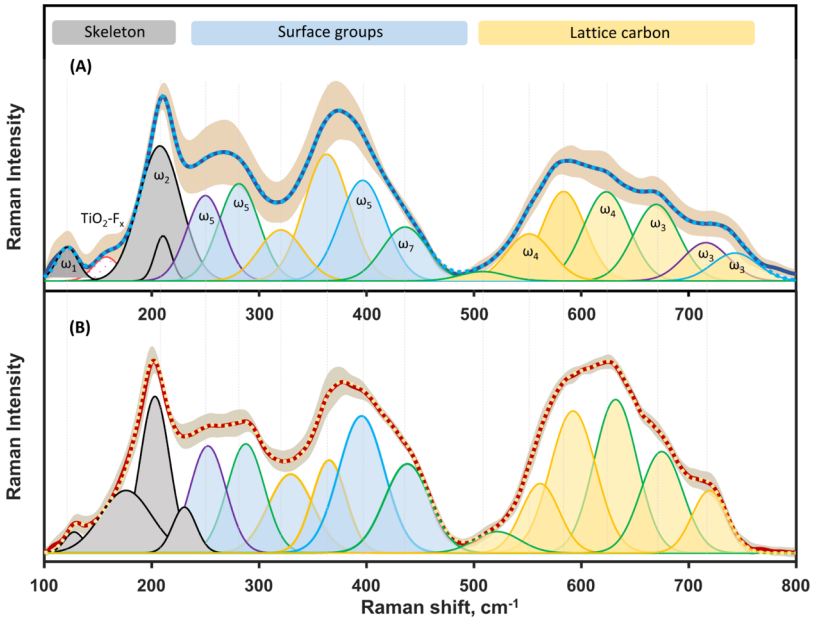

Figure 3. Deconvoluted Raman spectra in low-frequency (100−800 cm^{-1}) spectral region of multilayered (A) and single-layered $Ti_3C_2T_x$ MXene (B). The excitation wavelength was 633 nm. Spectra are separated into spectral regions: skeleton vibrations of all lattice atoms (gray); the surface group region that mainly consists of vibrations associated with the outermost atoms in the material (blue); the lattice carbon region that represents phonon modes of the carbon atoms (yellow). The peak profiles mark our proposed assignment of phonon modes from different homogeneously terminated $Ti_3C_2T_x$. Modes associated with $Ti_3C_2(OH)_2$ are outlined with the green line, $Ti_3C_2O_2$ with the blue line, $Ti_3C_2F_2$ with the violet line, and the complex peak profiles, constituting several MXene types, with the yellow line. The peak profile arising from Ti oxyfluoride is outlined with a pink line.

of synthesized MXene was investigated with SEM imaging (Figure 1). The stacked lamellae were observed in the $Ti_3C_2T_x$ multilayered MXene (Figure 1A,1B). After delamination, single-layered MXene flakes were formed and are shown in Figure 1C,D.

Delamination efficiency was confirmed by EDX analysis (Figure S1), which showed the presence of traces of aluminum, suggesting successful etching of the MAX phase and the formation of multilayered MXene. The aluminum residues were present as relatively uniform amorphous structures on the surface of the MXene sheets and did not affect the parameters investigated in this study. XRD analysis also confirmed the successful etching and delamination of the MXene samples (Figure 2B). The XRD patterns of synthesized MXene are presented in Figure 2B. The results clearly show that the MXene was synthesized, as indicated by the shift of the (002) peak to 7.0 and 7.1° in the case of multilayered and single-layered MXene, respectively.[60] However, the XRD pattern of multilayered MXene (Figure 2B) from 33 to 44° is similar to that of the MAX phase,[11] suggesting incomplete etching and/

https://doi.org/10.1021/acsnano.4c02150
ACS Nano 2024, 18, 13184−13195

or washing. In the case of single-layered MXene, two additional diffraction peaks at 38.7 and 45° are observed, which match the XRD data of LiF (00-004-0857) and indicate the presence of residual LiF after washing the MXene samples.

The differences between the multilayered and single-layered samples are also visible in the vis−NIR extinction spectra (Figure 2A). The spectra match the literature.[48]

The extinction spectrum of MXene, obtained after the delamination step, reveals an extinction band at ≈750 nm originating from interband transition.[20,48,61−63] Additionally, the extinction observed at wavelengths above 1100 nm has been previously assigned to plasmonic oscillations.[48,61] Our previous research reported increased energy losses, resulting from electronic transitions in the near-infrared (NIR) range for $Ti_3C_2T_x$ MXene.[11] Generally, the overlap between the plasmonic frequencies and electronic transitions leads to less pronounced and wide-band plasmon resonances,[64,65] which are observed in our case. The multilayered MXene is expected to have lower extinction in this range due to its lower charge-carrier density than single-layered MXene and different surface functional groups.

To conduct a comprehensive qualitative study of MXene, dried MXene films were separately stored in oxygen and nitrogen gas environments and investigated using both vis−NIR and Raman spectroscopy (Figures S2 and S3). The observed spectral differences between the freshly formed films and those stored in oxygen may be attributed to the partial oxidation of MXene. Previous studies have shown that the extent of oxidation depends on the oxygen content during storage[47,66,67] and temperature.[27]

Raman Spectroscopy Characterization of Single-Layered and Multilayered MXene. A further distinction between the single-layered and multilayered $Ti_3C_2T_x$ MXene can be made by vibrational spectroscopy, *e.g.*, by investigating Raman scattering. Generally, two spectral regions are important for Raman spectroscopic analysis of MXene: the low-frequency (100−800 cm^{-1}) one, which represents lattice vibrations (phonons), and the region from 1000 to 1800 cm^{-1}, which represents C−C stretching vibrations of carbon structures occurring in MXene films.

In the $Ti_3C_2T_x$ fingerprint region, the computational approach was able to provide mode assignments for homogeneously terminated MXene and explain the appearance of additional in-plane modes in MXene with heterogeneous terminations—two at approximately 300−400 cm^{-1} and two at 550−650 cm^{-1}. Our research incorporated these heterogeneous modes in the deconvoluted Raman profile of single-layered and multilayered MXene (Figure 3). Despite the difficulty in interpreting the Raman bands, the fitted Gaussian peak profiles align well with the proposed mode positions in this spectral region. Additionally, previous works suggested several markers for increasing =O content in MXene, such as blue shifts of the bands at approximately 700 and 395 cm^{-1} and a red shift of the band at approximately 620 cm^{-1}.[51] Correspondingly, in the case of voltage-induced oxidation of MXene, a red shift of the 620 cm^{-1} band and blue shift of the 395 cm^{-1} band were observed as well.[22,24,43,45]

Generally, Raman spectra of single-layered and multilayered MXene possess only minor differences. These differences might arise from various factors, including the number of synthesis steps,[42,43,47] variations in the interlayer spacing, and the presence of water and potential intercalants between the layers (Figure 3). The Raman spectra of multilayered MXene exhibit comparably lower intensity bands in the 560−800 cm^{-1} spectral region, which are mainly associated with the vibrations of the lattice carbon atoms. A notable reduction in intensity is observed for the complex band at approximately 620 cm^{-1}, which we mainly attribute to the in-plane vibrations of the carbon atoms. The complexity arises from different ratios of =O, −OH, and −F terminations affecting this and most other bands in MXene spectra. Several studies have shown that the red shift of this band indicates the oxidation of MXene.[22,45,51] Thus, in this research, we assigned the spectral region at approximately 590 cm^{-1} to $Ti_3C_2O_2$ MXene structures, while the region at approximately 667 cm^{-1} was assigned to $Ti_3C_2(OH)_2$ MXene structures (Table 1 and Figure 3).

Table 1. Experimentally Observed Raman Bands of Single-Layered and Multilayered $Ti_3C_2T_x$ MXene[a]

vibrational frequency, cm^{-1}				
single-layered		multilayered		
633 nm	785 nm	633 nm	785 nm	MXene type[49,51]
122	122[b]	122	123[b]	complex[49]
154	154	154	154	
200	201	211	210	complex[49]
256	258	258[c]	258	$Ti_3C_2F_2$[49,51]
283	283	284	283	$Ti_3C_2(OH)_2$[49]
372	372[b]	370	371[b]	complex[51]
450		452		$Ti_3C_2(OH)_2$[49]
511	513[b]	505[c]	512[b]	$Ti_3C_2(OH)_2$[49]
590	584	590	585	$Ti_3C_2O_2$[49,51]
626	617	621	616	complex[51]
667	667	667	668	$Ti_3C_2(OH)_2$[49,51]
712	722[b]	734	737[b]	$Ti_3C_2O_2$[49]
1396	1396			
1582	1582	1562	1561	

[a]Complex—two or more different MXene types. [b]Increased intensity in spectral band compared to 633 nm excitation. [c]Not prominent or weak band.

The most prominent contrast between the single-layered and multilayered MXene becomes evident in the band associated with the ω_2 mode (out-of-plane skeleton vibration of all atoms in the lattice, Table S1). The loosening of the ω_2 mode due to less confined out-of-plane vibrations in single-layered MXene leads to an observed red shift of the band from 211 to 200 cm^{-1} (Table 1). Similarly, a red shift is observed for the other out-of-plane vibrational modes at 734 cm^{-1} in multilayered MXene to 711 cm^{-1} in single-layered MXene. Notably, the latter band also shows sensitivity for the −O or −F content on the surface[51] and further underscores its dependence on the synthesis route.[42]

When comparing the Raman spectra of single-layered MXene collected using different excitation wavelengths, notable changes are observed primarily under preresonance conditions (Figure S4). From vis−NIR extinction spectra, the resonance Raman condition for MXene samples in our study was excitation with a wavelength of 750 nm (Figure 2). Excitation with a 785 nm laser provides photon energy close to the resonance Raman condition. The preresonance excitation yields Raman spectra with high intensity of a few resonant spectral bands (Figure S5). These bands include 122 cm^{-1} ("skeleton vibration"), which is associated with the in-plane vibrational mode of all atomic groups, 513 cm^{-1} (associated

https://doi.org/10.1021/acsnano.4c02150
ACS Nano 2024, 18, 13184−13195

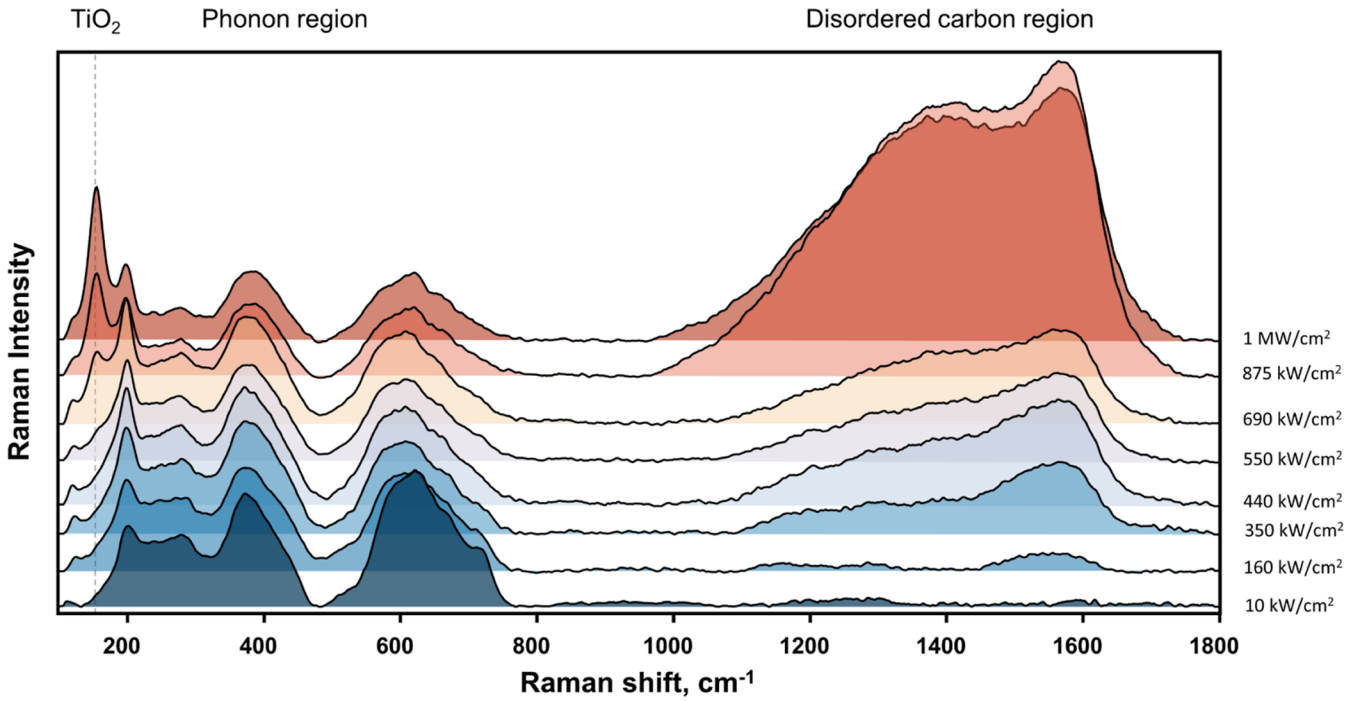

Figure 4. Changes in the Raman spectrum of $Ti_3C_2T_x$ are due to laser radiation. The laser power density varied from 10 kW/cm^2 to 1 MW/cm^2. Three spectral regions are marked as TiO_2 (spectral region of titanium oxide formation), phonon region (lower frequency vibrations), and disordered carbon region (vibrations of C−C bonds). The applied excitation wavelength was 633 nm.

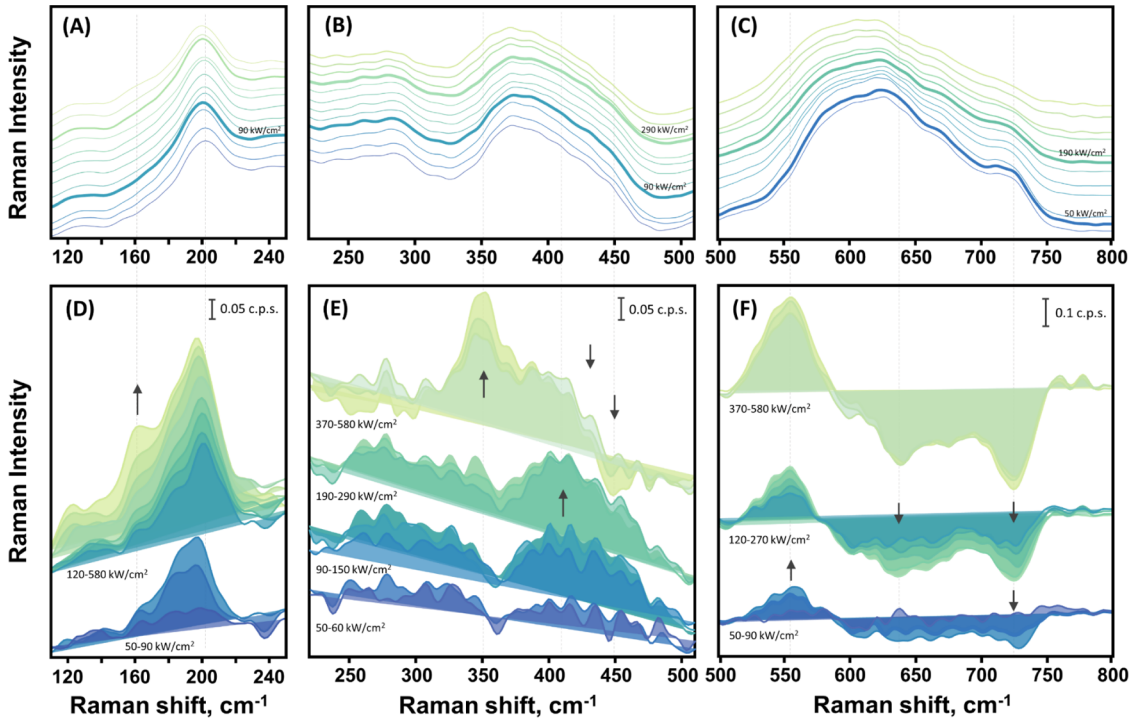

Figure 5. Low-frequency (100−800 cm^{-1}) Raman spectrum of deteriorating $Ti_3C_2T_x$ MXene due to 633 nm laser illumination (A−C) along with the corresponding differential spectra (D−F). The laser power density was changed: from 30, 50, 60; 90, 120, 150, 190, 230, 290, 370; and 470 to 580 kW/cm^2 with the spectra arranged from bottom to top in that order. To enhance clarity, the differential spectra, illustrating newly emerging spectral markers, are presented separately in the bottom panels. The arrows indicate changes in the spectra that emerge with an increasing laser power density. Data were smoothed with a Savitzky−Golay filter, and the unsmoothed spectra are shown in Figure S6.

with the out-of-plane ω_6 mode of $Ti_3C_2(OH)_2$), and 722 cm^{-1} (associated with the out-of-plane ω_3 mode of mainly $Ti_3C_2O_2$) bands.

Laser-Induced Disruption of MXene. The disruption of the MXene lattice was achieved by using different laser wavelengths: 633, 532, and 457 nm. Each laser generates a distinct power density on the sample and induces lattice

https://doi.org/10.1021/acsnano.4c02150
ACS Nano 2024, 18, 13184−13195

defects, which can be traced by Raman spectroscopy. The evolution of phonon bands was first examined using a 633 nm laser in the power density range of 10 kW/cm^2−1 MW/cm^2 (Figure 4). Additionally, samples were analyzed at a higher laser power density, which enables a rapid deterioration of the lattice, using a 532 nm laser (with the power density range of 20 kW/cm^2−26 MW/cm^2) and a 457 nm laser (with the power density range of 240 kW/cm^2−4.9 MW/cm^2) (Figures S7−S10). Comparable spectral patterns were observed for various excitation wavelengths at equivalent power densities. Reasons for MXene deterioration were previously identified and include (i) inner titanium (Ti) atom diffusion to outer layers in the presence of lattice defect; (ii) the formation of C−C bonds between different MXene planes; and (iii) the formation of TiO_2.[68]

The first apparent sign of lattice disruption in MXene can be seen in the disordered carbon spectral region of 1000−1800 cm^{-1} (Figure 4). Amorphous carbon and hydrocarbons begin to form at excitation powers of 160 kW/cm^2. Broad G and D bands can be observed at 1582 cm^{-1} (full width at half-maximum—fwhm of 300 cm^{-1}) and 1396 cm^{-1} (fwhm—120 cm^{-1}), respectively. The G band appears from C−C bond vibration in all sp^2 hybridized carbon systems, while the D band appears in disordered carbon ring systems.[69,70] Under 633 nm excitation, the intensity of the G band of disordered carbon continuously increased with increasing power density, reaching its maximum at 875 kW/cm^2. As the laser power density is further increased, the disordered carbon bands gradually weaken due to the widespread deterioration of C−C bonds, as shown in Figure 4.

The final and most abrupt step of MXene deterioration, namely, the formation of TiO_2 nanoparticles, was observed at a power density of 550 kW/cm^2 with 633 nm excitation. The formation was observed at lower power densities: 330 and 390 kW/cm^2 with 532 and 457 nm excitations, respectively, and advancing until approximately 1.5−1.6 MW/cm^2 (Figures S7−S10). TiO_2 formed from MXene can exist in two crystal structures: anatase and rutile. The anatase phase is the first to appear as it requires less energy to form. The anatase phase was identified by the most intense band at 154 cm^{-1} associated with the E_g mode. In our work, this mode appeared blue-shifted at low laser power densities, which is a sign of defects and oxygen deficiency in the anatase structure.[71−73] A higher content of anatase TiO_2 in the MXene sample is indicated by additional markers−spectral bands at 406 and 633 cm^{-1}, which are associated with B_{1g} and E_g modes, respectively, along with the red shift of E_g mode to 144 cm^{-1}. Further increasing the laser power density initiated the formation of the rutile phase of TiO_2. Spectral markers of the rutile phase start to dominate in the Raman spectra when the laser power density exceeds 2 MW/cm^2 (Figures S8−S10).

Low-Frequency Raman Spectrum of MXene Samples Subjected to Laser-Induced Disruption. Spectral changes of photodisrupted MXene are also observable in the phonon region of 100−800 cm^{-1} (Figure 5A−5C). Lattice vibrations were analyzed using laser excitation at a power density range of 30 to 580 kW/cm^2. More intense laser light severely disrupts the MXene layers. Therefore, the results for such samples are not included in the analysis. No significant differences were found when using various wavelengths for the excitation of Raman scattering (Figure S4). Consequently, we focus on the results obtained with 633 nm excitation (Figure 5).

The analysis of lattice phonon bands was conducted through differential spectra (Figure 5D−F). Initially, the spectrum obtained using the lowest laser power density was subtracted from the presented spectra. As the laser power density increased to 60 kW/cm^2, the 199 cm^{-1} spectral band, associated with the ω_2 mode, and the surface group bands increased in intensity, while the lattice carbon region became less intense. A slight red shift was observed in the 199 cm^{-1} band at 60 kW/cm^2, likely due to the heating of the sample. The upturn in laser power density to 90 kW/cm^2 revealed a pronounced blue shift for the ω_2 mode to 204 cm^{-1} (Figure 5A,D). Indeed, the blue shift is not expected and indicates the stiffening of the mode due to the removal of water molecules trapped between the MXene layers.[57,59] It has been shown that the loss of water and surface functional groups reduces the interlayer spacing, causing individual monolayers to converge,[9,56,58,59] though the loss of surface groups requires a higher temperature to desorb.[59]

In our study, we observed changes linked to increasing =O content in MXene[22,24,43,45] in addition to the reduction of interlayered water. Specifically, a blue shift in the complex band at 372 cm^{-1} was noted (Figure 5C). This blue shift was observed when the excitation power density was between 90 and 290 kW/cm^2, before anatase formation, indicating oxidation of the MXene.[24,42,43] The spectral region at 410 cm^{-1} displayed increased intensity within this power density range, which contributed to the observed blue shift in the 372 cm^{-1} band (Figure 5E). Another indication of oxidation is the red shift of the wide complex band at 626 cm^{-1}.[24] This red shift, peaking at 620 cm^{-1}, is noticeable in the spectra starting from 190 kW/cm^2 (Figure 5C). However, differential spectra reveal that changes in this area appeared much sooner. Furthermore, we observed the gradual increase of the band at 550 cm^{-1}, which is associated with $Ti_3C_2O_2$ structures in this work, together with a decrease of the band at 640 cm^{-1}, which we link to $Ti_3C_2(OH)_2$. These changes were observed even at a low laser power density of 50 kW/cm^2 and persisted as the power density reached 580 kW/cm^2 (Figure 5F). The decrease in the spectral region at 640 cm^{-1} became more pronounced at 190 kW/cm^2. Interestingly, we did not observe a blue shift of the band at 372 cm^{-1} when anatase was formed (when the sample was excited by 370 kW/cm^2 power density). However, we did observe a red shift of the complex band at 620 cm^{-1} in this case.

The bands at 283 and 256 cm^{-1} experience a rapid decrease starting at 370 kW/cm^2 (Figure 5B). The spectral band of anatase TiO_2 at 154 cm^{-1} appears together with the rapid growth of the band observed at 350 cm^{-1} when the sample is excited by a power density of 370 kW/cm^2. Other studies have reported that the band at 350 cm^{-1} is associated with the presence of −F the MXene.[43] However, our results suggest that the band at 350 cm^{-1} might be associated with the formation of TiO_2 structures, since they appear together.

Analyzing the intensity ratios of Raman bands associated with various vibrational modes of MXenes with different terminations can provide valuable insights into structural changes. This approach allows us to clearly distinguish indications of interlayer water reduction, MXene oxidation, and lattice disruptions. However, as previously mentioned, most of the MXene bands are complex; therefore, the assignments for these bands should be made with caution. This study focuses on analyzing the intensity changes of the most prominent MXene Raman bands. To enhance readability,

https://doi.org/10.1021/acsnano.4c02150
ACS Nano 2024, 18, 13184−13195

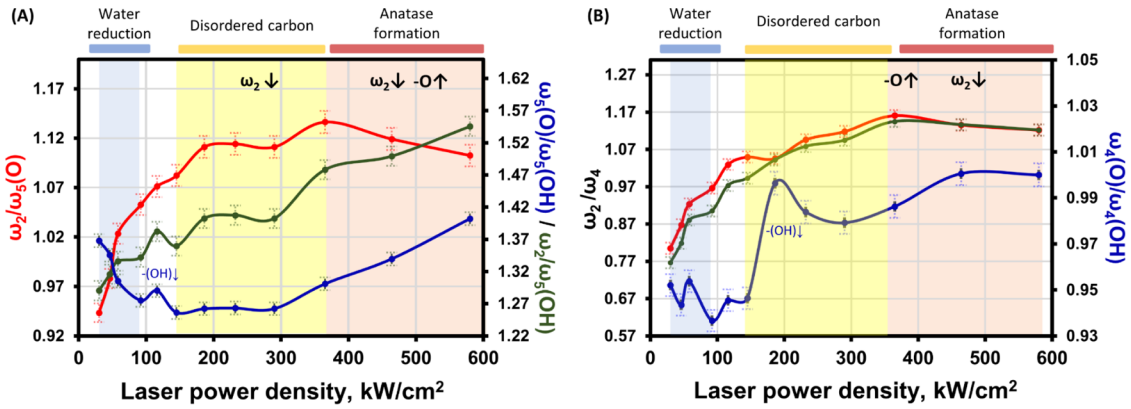

Figure 6. Intensity ratios of MXene Raman bands associated with different vibrational modes of $Ti_3C_2O_2$ and $Ti_3C_2(OH)_2$. The intensity ratios $I_{\omega 2}/I_{\omega 5(O)}$ (red line), $I_{\omega 2}/I_{\omega 5(OH)}$ (green line), and $I_{\omega 5(O)}/I_{\omega 5(OH)}$ (blue line) of ω_2 and ω_5 modes of either = O or −OH-terminated MXene (A). The intensity ratios $I_{\omega 2}/I_{4(O)}$ (red line), $I_{\omega 2}/I_{\omega 4(OH)}$ (green line), and $I_{\omega 4(O)}/I_{\omega 4(OH)}$ (blue line) of ω_2 and ω_4 modes of either ═O or −OH-terminated MXene (B). The main changes in the MXene lattice are noted above the graph: −O↑—increasing oxidation; ω_2↓—reduction of the ω_2 mode intensity. The main processes distinguished by spectral markers appearing in the spectra are noted above the graphs: reduction of interlayered water, formation of disordered carbon bands, and formation of anatase.

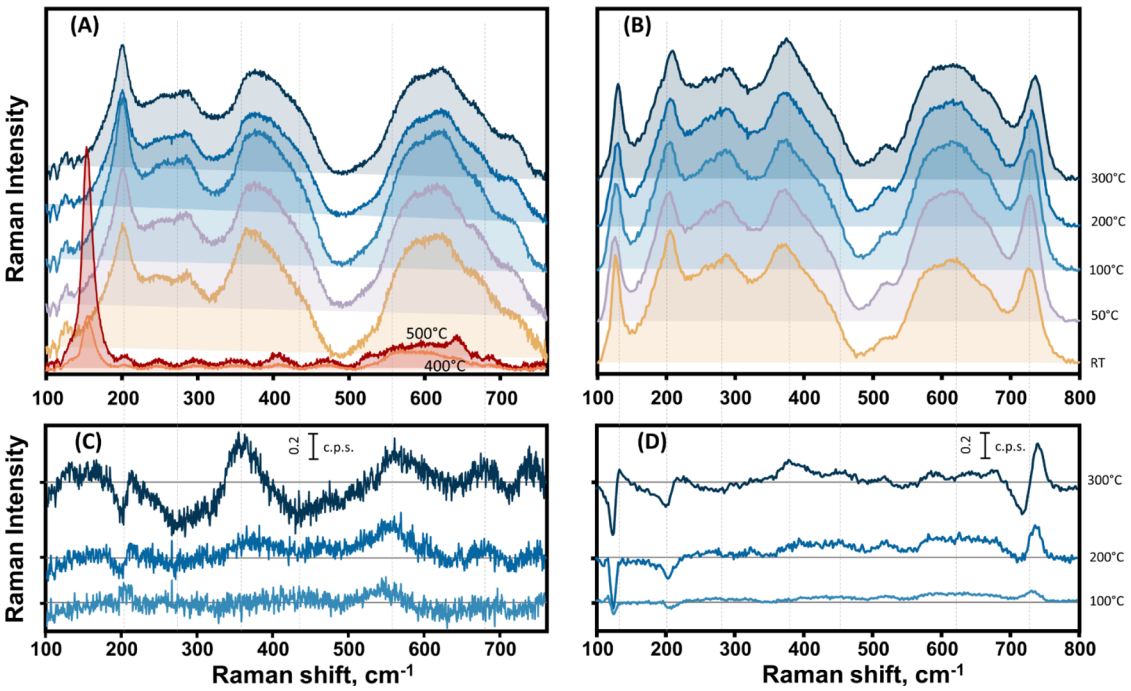

Figure 7. Raman spectra in the phonon spectral region (100−800 cm^{-1}) of $Ti_3C_2T_x$-based MXene deteriorating due to heating. Raman excitation wavelengths were 633 nm (A) and 785 nm (B). Subtracted spectra are presented in (C, D) at excitation wavelengths of 633 and 785 nm, respectively. MXene treatment temperatures of 50, 100, 200, and 300 °C are indicated at the right axis of the figure. Spectra recorded after heating to 400 and 500 °C are shown in (A).

we made tentative assignments of these bands to the lattice modes of $Ti_3C_2O_2$ and $Ti_3C_2(OH)_2$.

Specifically, we calculated the intensity ratios of the ω_2 mode and the peaks at 372 or 283 cm^{-1}, which were related to the ω_5 modes of either ═O-terminated MXene ($I_{\omega 2}/I_{\omega 5(O)}$) or −OH-terminated MXene ($I_{\omega 2}/I_{\omega 5(OH)}$), respectively. Given the complexity of the bands, we also considered other ratios between the ω_2 mode and peaks at 590 or 626 cm^{-1}, assigned to the ω_4 modes of = O-terminated MXene ($I_{\omega 2}/I_{\omega 4(O)}$), or −OH-terminated MXene $I_{\omega 2}/I_{\omega 4(OH)}$ as complementary information. These intensity ratios offered insights into the changes in surface groups.

In general, the intensity of the ω_2 mode increases with an increasing power density at low levels. The $I_{\omega 5(O)}/I_{\omega 5(OH)}$ ratio, on the other hand, decreased from 1.37 to 1.26 (at 150 kW/cm^2) and then began increasing at 370 kW/cm^2, reaching 2.1 (at 1 MW/cm^2) (Figure 6A, blue curve). The decrease in the $I_{\omega 5(O)}/I_{\omega 5(OH)}$ ratios at low laser power densities could be explained by the changes in interlayer spacing from the water in the sample. This correlates to the blue shift of the ω_2 mode at 90 kW/cm^2, indicating the water reduction. After the complete water reduction (at 120 kW/cm^2 laser power density), the amount of −OH surface groups decreases, as was observed in annealing studies.[57] It is marked by a bump in the green and blue curves in Figure 6A at 120 kW/cm^2

https://doi.org/10.1021/acsnano.4c02150
ACS Nano 2024, 18, 13184−13195

together with a rapid increase in the $I_{\omega4(O)}/I_{\omega4(OH)}$ ratio from 0.95 to 1.00 at 190 kW/cm^2 (Figure 6B, blue curve).

Following this process, lattice deterioration becomes evident from 150 kW/cm^2 by the onset of C−C formation, as indicated by the appearance of spectral bands related to disordered carbon (Figure 4). This deterioration is characterized by a decrease in the $I_{\omega2}/I_{\omega5(OH)}$ and $I_{\omega5(O)}/I_{\omega5(OH)}$ ratios. Notably, the $Ti_3C_2(OH)_2$ MXene is supposed to be the least stable.[57] Another sign of $Ti_3C_2(OH)_2$ diminishing is evidenced by the sharp increase in the $I_{\omega4(O)}/I_{\omega4(OH)}$ at 190 kW/cm^2. The decrease in $I_{\omega4(O)}/I_{\omega4(OH)}$ ratio (Figure 6B, blue curve) is observed for the range 190−290 kW/cm^2, which coincides with the increasing intensity of disordered carbon bands and indicates further lattice deterioration.

The sudden rise in $I_{\omega2}/I_{\omega5(O)}$, $I_{\omega2}/I_{\omega5(OH)}$, together with a rise in $I_{\omega5(O)}/I_{\omega5(OH)}$ and $I_{\omega4(O)}/I_{\omega4(OH)}$ ratios at 370 kW/cm^2 indicates the initiation of anatase formation and further oxidation of the $Ti_3C_2T_x$ MXene, presumably signifying the diminishing of surface groups. As oxidation progresses (with increasing laser power density), the most noticeable change is the decreasing $I_{\omega2}/I_{\omega5(O)}$ ratio. Interestingly, the marker for lattice degradation just before the appearance of the anatase band (characterized by a bump at 154 cm^{-1} in the spectra) can be observed from these ratios, as well. The $I_{\omega2}/I_{\omega5(O)}$ and $I_{\omega2}/I_{\omega5(OH)}$ ratios show a slight decrease just before the appearance of the anatase band in the spectra (at 290 kW/cm^2).

Impact of Annealing Temperature on MXene Samples. Temperature-induced changes in the MXene lattice occur at elevated temperatures. As previously mentioned, the thermal effect alters both the surface functional groups and the lattice structure of the MXene while reducing the number of water molecules trapped between the monolayers.[9,56−58,74] To distinguish between reversible and irreversible lattice changes, MXene films were dried on a SiO_2-based substrate and then annealed at various temperatures from 50 to 500 °C. The efficiency of these effects can be investigated using the Raman spectra of annealed MXene samples. To accomplish this, Raman spectra were obtained with preresonance (785 nm) and nonresonance (633 nm) excitations before and after annealing.

Almost no difference was observed when comparing the Raman spectra of the sample before and after heating to 50 °C (Figure 7A,7C). However, a significant increase in the intensities of the wide G and D bands in the carbon spectral region at 1582 and 1396 cm^{-1} is observed as the temperature increases from 200 to 300 °C (Figure S11). When the MXene sample is heated to 400 °C, the intensities of the carbon spectral bands decrease and a new band belonging to the defective TiO_2 anatase phase appears at 154 cm^{-1}. At 500 °C, no carbon bands are detected, and only anatase bands at 154, 406, and 633 cm^{-1} are observed (Figure 7A).

In the phonon spectral region of the MXene sample, almost no spectral changes are observed after heating at 50 °C, except for a slight increase in intensity of the 201 cm^{-1} band, which may indicate the initiation of reduction of interlayered water, as discussed earlier.[56] The shifts in phonon bands, regarded as spectral markers for a reduction in interlayered molecules, were not discernible for 633 nm excitation (Figure 7C). Heating to 300 °C resulted in red shifts of surface termination bands from 372 to 368 cm^{-1} (associated with MXene oxidation) and from 256 to 246 cm^{-1}. The latter shift correlates with an intensity drop at 283 cm^{-1} (Figure 7C). We related this red shift to the decrease in −(OH) surface groups due to several factors: $Ti_3C_2(OH)_2$ is supposed to be less stable and degrade first,[57] and the computational studies of MXene indicate the presence of $Ti_3C_2F_2$ vibrational mode in this spectral range with generally stable mode position.[49,51] It is worth mentioning that contrary to the laser-induced study, no blue shift of the 372 cm^{-1} band or signal increase at 410 or 450 cm^{-1} was observed during annealing.

The excitation at 785 nm provides complementary results (Figure 7B,7D). Annealing at 50 and 200 °C resulted in a coincident blue shift of the ω_2 mode from 201 to 208 cm^{-1}, respectively. Noticeable changes compared with excitation at 633 nm were observed for the resonant bands at 722 and 122 cm^{-1} (Table 1). These bands show gradual blue shifts from 722 to 734 cm^{-1} and from 122 to 127 cm^{-1} as the temperature increases from 50 to 300 °C. The blue shift of the bands at 122 and 202 cm^{-1} may indicate the removal of interlayer water.

Based on the results of the laser-induced study, several irreversible changes in the MXene lattice were observed. First, a reduction in interlayered water was observed from 200 °C, as indicated by the blue shift of the ω_2 mode. Second, the band at approximately 626 cm^{-1} was red-shifted to 550 cm^{-1}, indicating oxidation of the MXene, starting from 100 °C. Third, further oxidation was indicated by a decrease in intensity of the band at approximately 280 cm^{-1}, accompanied by an increase in intensity of the band at 372 cm^{-1} (for MXene heated at 200 °C). Fourthly, progressing oxidation was indicated by a significant decrease in the bands at 283 cm^{-1}, at ∼435 cm^{-1}, and at 626 cm^{-1} (associated with the $Ti_3C_2(OH)_2$ MXene) and an increase in intensity at 550 cm^{-1} (associated with the oxidation of MXene structure). Lastly, a new band at 154 cm^{-1} was observed for MXene heated at 400 °C, indicating the formation of anatase TiO_2.

DISCUSSION

While we observed significant spectral changes following MXene film treatments (both laser-induced and heat-induced degradation), interpretation of these changes is challenging due to the lack of computational validation for heterogeneous surface terminations. However, these spectral changes are consistent with the results of other annealing and MXene treatment studies.[22,45,51,57]

The spectral changes during the MXene film treatment with a laser were observed and can be outlined in several steps. (I) The reduction of interlayered molecules (together with water) was observed from the blue shift of the band at 200 cm^{-1} at low power densities. (II) A further increase in power density resulted in reduction in surface groups. We hypothesize that this reduction can be inferred from the blue shift of the 370 cm^{-1} band coupled with a spike in the $I_{\omega2}/I_{\omega4(OH)}$ ratio, indicating a decrease in −(OH) surface groups.[49] Another indication of oxidation, the red shift of the 620 cm^{-1} band, was noticed at higher power densities but was visible even during the formation of TiO_2 structures. These spectral markers indicate changes in surface groups, allowing us to pinpoint when these changes initiate. The blue shift of the 370 cm^{-1} band is observed first, though it only occurs at lower power densities. Differential spectra unveil subtler changes occurring even at lower laser power densities for the 620 cm^{-1} band. We observed a gradual increase in the band at 550 cm^{-1}, which was accompanied by a decrease in the band at 640 cm^{-1}. These changes were noticeable, even at a low laser power density of 50 kW/cm^2. (III) The formation of the C−C bonds occurred due to defects in the lattice structure. (IV) TiO_2 structures started to form. It was noted that the reduction of surface

https://doi.org/10.1021/acsnano.4c02150
ACS Nano 2024, 18, 13184−13195

groups was intertwined with the formation of C−C bonds and the beginning of the formation of TiO_2 structures.

During the thermal treatment of MXene films, the most pronounced spectral changes occurred for samples heated to 200−300 °C. A red shift of the band at ∼620 cm^{-1} was observed as a sign of oxidation, but no blue shift of the band at ∼370 cm^{-1} was observed. However, a red shift of the latter band was observed for samples heated to 300 °C. It is important to note that in the study of laser-induced deterioration of MXene, the blue shift of the 370 cm^{-1} band was visible only until the formation of anatase began, after which a red shift was observed likewise. Based on the mode assignments of the homogeneous MXene, we can infer that the significant decrease in the bands at approximately 283, 435, and 620 cm^{-1} is associated with the $Ti_3C_2(OH)_2$ MXene. Heating to 400 °C or above destroyed the MXene lattice. It should be noted that heating was conducted in a furnace and not under vacuum conditions. In the case of vacuum annealing, it is expected that carbon bands would still be visible at higher temperatures due to the absence of oxygen.

The differences in MXene degradation observed with laser and thermal treatments could be attributed to more severe temperature changes or different treatment conditions. In the furnace, the temperature is uniformly distributed across the entire sample. However, when heating with a laser, there is a significant temperature difference between the laser spot and the surrounding area. Another important difference to consider is the heating duration of the samples in the furnace, which was 30 min, while the laser treatment was limited to 5−10 min. As a result, the trends for disordered carbon and anatase formation were different.

The previously identified spectral changes induced by MXene lattice deterioration, caused by laser or thermal treatment, can be adapted to determine the MXene film aging. MXene films aged in oxygen and nitrogen environments differ from each other (Figure S3). The film kept in an oxygen environment is supposed to oxidize, increasing the number of =O surface functional groups. Indeed, the blue shift of the complex band at 372 cm^{-1} was only observed for MXene aged in an oxygen environment. However, the formation of TiO_2 was not observed from the Raman spectra.

CONCLUSIONS

This study focused on exploring lattice transitions in $Ti_3C_2T_x$ MXene evoked by thermal and laser treatments using Raman spectroscopy as the primary analytical technique. In the laser-induced degradation study, the out-of-plane mode shifted with reduction in the interlayer water at lower power densities, followed by a blue shift of the band associated with the increasing =O content and diminishing of the bands of −OH-terminated MXenes. Amorphous carbon and hydrocarbons formed at excitation powers of 160 kW/cm^2, while the formation of TiO_2 nanoparticles (first the anatase phase, followed by a rutile phase) was observed at a power density of 550 kW/cm^2 with 633 nm excitation wavelength. In the heating process, exposure to 100 °C led to a red shift of the out-of-plane mode, indicating the initiation of oxidation processes, while more pronounced oxidation and interlayer water reduction markers were observed at 200−300 °C. Finally, at 400 °C, a new band indicated the formation of anatase TiO_2. Unlike laser treatment, no blue shift in certain bands was observed, indicating distinct degradation mechanisms under thermal conditions.

The findings presented here enhance the integration of Raman spectroscopy into MXene analysis by increasing our understanding of degradation pathways *via* related spectral markers. The critical optical and electric properties of MXene depend on structural changes, oxidation state, and the presence of amorphous carbon; thereby, the relation of Raman markers to degradation stages provides an invaluable tool for quickly assessing the structure of MXene. Further use of this knowledge enables the application of MXenes as components in more complex material structures while continuing to employ fast and straightforward Raman spectroscopy for characterization and analysis.

EXPERIMENTAL SECTION

Synthesis of Multilayered $Ti_3C_2T_x$ MXene Colloidal Solutions. MXene used in this study was synthesized by selective etching Al layers from a Ti_3AlC_2 (Materials Research Center Ltd.; ≤40 μm particle size) MAX phase precursor. Detailed synthesis of multilayered $Ti_3C_2T_x$ MXene proceeded as described elsewhere.[11] Briefly, 0.1 g of Ti_3AlC_2 was gradually added to 5 wt % hydrofluoric acid (HF, Honeywell, 40 wt %, ACS, 7664-39-3) solution. The mixture was stirred at 200 rpm/min and kept on a thermostat for 24 h at 25 °C. After etching, the products were washed from the residues of acid with Milli-Q water by centrifugation in plastic centrifuge tubes at 2550 rcf for 10 min until the clear supernatant reached neutral pH. The sediments collected during centrifugation were multilayered $Ti_3C_2T_x$ MXene.

Synthesis of Single-Layered $Ti_3C_2T_x$ MXene. To obtain single-layered MXene using the minimally intensive layer delamination (MILD) method,[60] 0.1 g of Ti_3AlC_2 was gradually added to the 9 M hydrochloric acid (HCl, Roth, 37 wt %, ACS, 7647−01−0) solution with dissolved 1 g of LiF (Roth, >99%, 7789−24−4). The mixture was stirred at 200 rpm/min and kept on a thermostat for 48 h at 35 °C. The products were washed with Milli-Q water by centrifugation in plastic centrifuge tubes 3 times until the supernatant became dark, which indicates delamination. Then, centrifugation was continued, and a dark supernatant with delaminated, single-layered $Ti_3C_2T_x$ MXene was collected. All substrates analyzed in this study were prepared by drop-casting of 0.01 g/mL solution of MXene on microscopic glass.

Characterization of MXene Structures. $Ti_3C_2T_x$ MXene morphology and elemental composition were evaluated by a scanning electron microscope Helios Nanolab 650 (FEI, Eindhoven, Netherlands) equipped with an EDX spectrometer X-Max (Oxford Instruments, Abingdon, U.K.). X-ray diffraction analysis was executed using Ni-filtered Cu Kα radiation on a MiniFlex II diffractometer (Rigaku, Tokyo, Japan) in Bragg−Brentano ($\theta/2\theta$) geometry within 2θ angle ranging from 5 to 60° with a step width of 0.02° and a sweep rate of 1°/min.

Optical characterization of MXene was performed using Vis−NIR and vibrational Raman spectroscopy. Extinction spectra were acquired in the spectral region 450−2300 nm using a Lambda 1050 UV−vis−NIR spectrophotometer (PerkinElmer). A MonoVista CRS+ Raman microscope (Spectroscopy & Imaging GmbH, Germany) equipped with 457, 532, 633, and 785 nm excitation lasers, 100×/0.8 NA objective, and a liquid nitrogen-cooled CCD detector was used for Raman analysis. All Raman spectra were collected using a 300 s exposure time. A 1500 lines/mm grating was employed to collect all spectra except those acquired with 785 nm excitation and for the 633 nm excitation, where a 300 lines/mm grating was used to cover the 100−1800 cm^{-1} spectral range. Before the measurements, the spectrometer was calibrated to the fundamental vibrational band of a silicon wafer at 520.7 cm^{-1}.

For Raman spectroscopic analysis, the laser power was kept at ≈0.4 mW, which ensures a laser power density of ≈60 kW/cm^2. The laser power was adjusted for the laser-induced deterioration study and is specified in the Results Section. The data in the deconvoluted Raman spectra and the low-frequency (100−800 cm^{-1}) Raman spectrum of

https://doi.org/10.1021/acsnano.4c02150
ACS Nano 2024, 18, 13184−13195

deteriorating $Ti_3C_2T_x$ MXene in Figure 5 were smoothed using a Savitzky−Golay filter with a 9-point window. The unsmoothed spectra are provided in the Supporting Information.

For the evaluation of successful MXene synthesis, Raman mapping was conducted across a 10 × 10 μm^2 area of the sample with a 1 μm step and no spectral markers of the MAX phase were observed. Additionally, both EDX and XRD analyses showed no trace of the MAX phase.

Assessment of MXene Stability. The prepared MXene samples were subjected to different treatments: thermal annealing and storage under various conditions. For thermal annealing, the samples were placed in a furnace (Zhermack DM 40, Badia Polesine, Italy) by holding at 50, 100, 200, 300, 400, and 500 °C for 30 min. To study the stability of MXene under different storage conditions, MXene films were placed in a cuvette that was flushed and subsequently filled with dry oxygen or nitrogen gas and stored for 1 week at room temperature.

ASSOCIATED CONTENT

Supporting Information

The Supporting Information is available free of charge at https://pubs.acs.org/doi/10.1021/acsnano.4c02150.

EDX mapping images of single-layered $Ti_3C_2T_x$ MXene flakes; vis−NIR extinction, Raman spectra and corresponding analysis of single-layered MXene flakes separately stored in oxygen and nitrogen gas environments; Raman spectra, analysis, and band assignment table of single-layered MXene obtained with different excitation wavelengths; Raman spectra of multilayered and single-layered MXene excited with 785 nm laser; Raman spectra of deteriorating Mxene due to laser illumination (457, 532, 633 nm) and due to heating (PDF)

AUTHOR INFORMATION

Corresponding Authors

Sonata Adomaviciute-Grabusove − *Institute of Chemical Physics, Vilnius University, LT-10257 Vilnius, Lithuania*; Email: sonata.adomaviciute@ff.vu.lt

Simonas Ramanavicius − *Department of Organic Chemistry, Centre for Physical Sciences and Technology, LT-10257 Vilnius, Lithuania*; Email: simonas.ramanavicius@ftmc.lt

Arunas Ramanavicius − *Department of Physical Chemistry, Institute of Chemistry, Faculty of Chemistry and Geosciences, Vilnius University, LT-03225 Vilnius, Lithuania; Department of Nanotechnology, Centre for Physical Sciences and Technology, LT-10257 Vilnius, Lithuania*; orcid.org/0000-0002-0885-3556; Email: arunas.ramanavicius@chf.vu.lt

Authors

Anton Popov − *NanoTechnas—Center of Nanotechnology and Materials Science, Institute of Chemistry, Faculty of Chemistry and Geosciences, Vilnius University, LT-03225 Vilnius, Lithuania*; orcid.org/0000-0002-9867-1931

Valdas Sablinskas − *Institute of Chemical Physics, Vilnius University, LT-10257 Vilnius, Lithuania*

Kateryna Shevchuk − *A.J. Drexel Nanomaterials Institute and Materials Science & Engineering Department, Drexel University, Philadelphia, Pennsylvania 19104, United States*; orcid.org/0000-0001-7411-3110

Oleksiy Gogotsi − *Materials Research Center, Ltd., 03142 Kyiv, Ukraine*; orcid.org/0000-0002-3173-4432

Ivan Baginskiy − *Materials Research Center, Ltd., 03142 Kyiv, Ukraine*; orcid.org/0000-0002-0092-9018

Yury Gogotsi − *A.J. Drexel Nanomaterials Institute and Materials Science & Engineering Department, Drexel University, Philadelphia, Pennsylvania 19104, United States*

Complete contact information is available at: https://pubs.acs.org/10.1021/acsnano.4c02150

Notes

The authors declare no competing financial interest.

ACKNOWLEDGMENTS

This project has received funding from the Research Council of Lithuania (LMTLT), agreement No S-PD-22-155. Research at Drexel University was supported by a U.S. National Science Foundation grant (DMR-2041050) and EU Horizon Europe research program projects #101131147 "ESCULAPE" and #101086184 "MX-MAP". The authors are grateful to Dr. Arnas Naujokaitis for scanning electron microscopy imaging.

REFERENCES

(1) Naguib, M.; Kurtoglu, M.; Presser, V.; Lu, J.; Niu, J.; Heon, M.; Hultman, L.; Gogotsi, Y.; Barsoum, M. W. Two-Dimensional Nanocrystals Produced by Exfoliation of Ti_3AlC_2. *Adv. Mater.* **2011**, *23* (37), 4248−4253.

(2) Anasori, B.; Gogotsi, Y. *2D Metal Carbides and Nitrides (MXenes)*; Springer: Cham, 2019.

(3) Bhat, A.; Anwer, S.; Bhat, K. S.; Mohideen, M. I. H.; Liao, K.; Qurashi, A. Prospects Challenges and Stability of 2D MXenes for Clean Energy Conversion and Storage Applications. *npj 2D Mater. Appl.* **2021**, *5* (1), No. 61.

(4) Papadopoulou, K. A.; Chroneos, A.; Parfitt, D.; Christopoulos, S.-R. G. A Perspective on MXenes: Their Synthesis, Properties, and Recent Applications. *J. Appl. Phys.* **2020**, *128* (17), No. 170902.

(5) Anasori, B.; Lukatskaya, M. R.; Gogotsi, Y. 2D Metal Carbides and Nitrides (MXenes) for Energy Storage. *Nat. Rev. Mater.* **2017**, *2* (2), No. 16098.

(6) Gogotsi, Y.; Anasori, B. The Rise of MXenes. *ACS Nano* **2019**, *13* (8), 8491−8494.

(7) Li, J.; Levitt, A.; Kurra, N.; Juan, K.; Noriega, N.; Xiao, X.; Wang, X.; Wang, H.; Alshareef, H. N.; Gogotsi, Y. MXene-Conducting Polymer Electrochromic Microsupercapacitors. *Energy Storage Mater.* **2019**, *20*, 455−461.

(8) Zhang, D.; Wang, R.; Wang, X.; Gogotsi, Y. In Situ Monitoring Redox Processes in Energy Storage Using UV−Vis Spectroscopy. *Nat. Energy* **2023**, *8* (6), 567−576.

(9) Xie, Y.; Naguib, M.; Mochalin, V. N.; Barsoum, M. W.; Gogotsi, Y.; Yu, X.; Nam, K.-W.; Yang, X.-Q.; Kolesnikov, A. I.; Kent, P. R. C. Role of Surface Structure on Li-Ion Energy Storage Capacity of Two-Dimensional Transition-Metal Carbides. *J. Am. Chem. Soc.* **2014**, *136* (17), 6385−6394.

(10) Bai, W.; Xiao, C.; Xie, Y. Bulk Superlattice Analogues for Energy Conversion. *J. Am. Chem. Soc.* **2022**, *144* (8), 3298−3313.

(11) Adomavičiūtė-Grabusovė, S.; Ramanavičius, S.; Popov, A.; Šablinskas, V.; Gogotsi, O.; Ramanavičius, A. Selective Enhancement of SERS Spectral Bands of Salicylic Acid Adsorbate on 2D $Ti_3C_2T_x$-Based MXene Film. *Chemosensors* **2021**, *9* (8), No. 223.

(12) Wang, Y.; Yue, Y.; Cheng, F.; Cheng, Y.; Ge, B.; Liu, N.; Gao, Y. $Ti_3C_2T_x$ MXene-Based Flexible Piezoresistive Physical Sensors. *ACS Nano* **2022**, *16* (2), 1734−1758.

(13) Wu, Z.; Wei, L.; Tang, S.; Xiong, Y.; Qin, X.; Luo, J.; Fang, J.; Wang, X. Recent Progress in $Ti_3C_2T_x$ MXene-Based Flexible Pressure Sensors. *ACS Nano* **2021**, *15* (12), 18880−18894.

(14) Yadav, P.; Cao, Z.; Farimani, A. B. DNA Detection with Single-Layer Ti_3C_2 MXene Nanopore. *ACS Nano* **2021**, *15* (3), 4861−4869.

(15) Jing, H.; Zhao, P.; Liu, C.; Wu, Z.; Yu, J.; Liu, B.; Su, C.; Lei, W.; Hao, Q. Surface-Enhanced Raman Spectroscopy for Boosting Electrochemical CO_2 Reduction on Amorphous-Surfaced Tin Oxide Supported by MXene. *ACS Appl. Mater. Interfaces* **2023**, *15* (51), 59524−59533.
(16) Ratzker, B.; Messer, O.; Favelukis, B.; Kalabukhov, S.; Maman, N.; Ezersky, V.; Sokol, M. MXene-Based Ceramic Nanocomposites Enabled by Pressure-Assisted Sintering. *ACS Nano* **2023**, *17* (1), 157−167.
(17) Yue, Y.; Liu, N.; Ma, Y.; Wang, S.; Liu, W.; Luo, C.; Zhang, H.; Cheng, F.; Rao, J.; Hu, X.; Su, J.; Gao, Y. Highly Self-Healable 3D Microsupercapacitor with MXene−Graphene Composite Aerogel. *ACS Nano* **2018**, *12* (5), 4224−4232.
(18) Lee, J.; Hong, S.; Sun, Y.; Lee, S. K.; Hwang, U.; Nam, J.-d.; Suhr, J. Parasitic Reaction Driven Facile Preparation of Segregated-MXene/Polycarbonate Nanocomposites for Efficient Electromagnetic Interference Shielding. *Surf. Interfaces* **2023**, *40*, No. 103101.
(19) Weng, X.; Weng, Z.; Qin, M.; Zhang, J.; Wu, Y.; Jiang, H. Bioinspired Moisture-Driven Soft Actuators Based on MXene/Aramid Nanofiber Nanocomposite Films. *ACS Appl. Nano Mater.* **2024**, *7* (5), 5587−5597.
(20) Hantanasirisakul, K.; Zhao, M.-Q.; Urbankowski, P.; Halim, J.; Anasori, B.; Kota, S.; Ren, C. E.; Barsoum, M. W.; Gogotsi, Y. Fabrication of $Ti_3C_2T_x$ MXene Transparent Thin Films with Tunable Optoelectronic Properties. *Adv. Electron. Mater.* **2016**, *2* (6), No. 1600050.
(21) Mistry, H.; Varela, A. S.; Kühl, S.; Strasser, P.; Cuenya, B. R. Nanostructured Electrocatalysts with Tunable Activity and Selectivity. *Nat. Rev. Mater.* **2016**, *1* (4), No. 16009.
(22) Johnson, D.; Hansen, K.; Yoo, R.; Djire, A. Elucidating the Charge Storage Mechanism on Ti_3C_2 MXene through In Situ Raman Spectroelectrochemistry. *ChemElectroChem* **2022**, *9* (18), No. e202200555.
(23) Lee, S.; Kim, E. H.; Yu, S.; Kim, H.; Park, C.; Lee, S. W.; Han, H.; Jin, W.; Lee, K.; Lee, C. E.; Jang, J.; Koo, C. M.; Park, C. Polymer-Laminated $Ti_3C_2T_x$ MXene Electrodes for Transparent and Flexible Field-Driven Electronics. *ACS Nano* **2021**, *15* (5), 8940−8952.
(24) Li, H.; Chen, S.; Boukhvalov, D. W.; Yu, Z.; Humphrey, M. G.; Huang, Z.; Zhang, C. Switching the Nonlinear Optical Absorption of Titanium Carbide MXene by Modulation of the Surface Terminations. *ACS Nano* **2022**, *16* (1), 394−404.
(25) Maleski, K.; Ren, C. E.; Zhao, M.-Q.; Anasori, B.; Gogotsi, Y. Size-Dependent Physical and Electrochemical Properties of Two-Dimensional MXene Flakes. *ACS Appl. Mater. Interfaces* **2018**, *10* (29), 24491−24498.
(26) Chertopalov, S.; Mochalin, V. N. Environment-Sensitive Photoresponse of Spontaneously Partially Oxidized Ti_3C_2 MXene Thin Films. *ACS Nano* **2018**, *12* (6), 6109−6116.
(27) Ghassemi, H.; Harlow, W.; Mashtalir, O.; Beidaghi, M.; Lukatskaya, M. R.; Gogotsi, Y.; Taheri, M. L. In Situ Environmental Transmission Electron Microscopy Study of Oxidation of Two-Dimensional Ti_3C_2 and Formation of Carbon-Supported TiO_2. *J. Mater. Chem. A* **2014**, *2* (35), 14339−14343.
(28) Hong, J.; Paeng, C.; Park, S.; In, I.; Lee, H.; Velhal, N. B.; Yun, T. H.; Jo, C.; Yim, C. Flashlight Treatment for Instantaneous Structuring of Dense MXene Film into Porous MXene/TiO_2 Nanocomposite for Lithium-Ion Battery Anodes. *Chem. Eng. J.* **2024**, *484*, No. 149598.
(29) Kumar, S.; Aftab, S.; Singh, T.; Kumar, M.; Kumar, S.; Seo, Y. Charge Storage Improvement in Uniformly Grown TiO_2 on $Ti_3C_2T_x$ MXene Surface. *J. Alloys Compd.* **2023**, *968*, No. 172181.
(30) Liu, Y.; Zhang, H.; Zhu, D.; Duan, J.; Miruka, A. C.; Tang, L.; Li, P.; Cai, L. Enhanced Degradation of Tetracycline by TiO_2 @ MXene with Peroxydisulfate under Visible Light Irradiation. *Sep. Purif. Technol.* **2024**, *343*, No. 127122.
(31) Mathis, T. S.; Maleski, K.; Goad, A.; Sarycheva, A.; Anayee, M.; Foucher, A. C.; Hantanasirisakul, K.; Shuck, C. E.; Stach, E. A.; Gogotsi, Y. Modified MAX Phase Synthesis for Environmentally Stable and Highly Conductive Ti_3C_2 MXene. *ACS Nano* **2021**, *15* (4), 6420−6429.
(32) Zhang, C. J.; Pinilla, S.; McEvoy, N.; Cullen, C. P.; Anasori, B.; Long, E.; Park, S.-H.; Seral-Ascaso, A.; Shmeliov, A.; Krishnan, D.; Morant, C.; Liu, X.; Duesberg, G. S.; Gogotsi, Y.; Nicolosi, V. Oxidation Stability of Colloidal Two-Dimensional Titanium Carbides (MXenes). *Chem. Mater.* **2017**, *29* (11), 4848−4856.
(33) Kumar, S.; Park, H. M.; Nguyen, V. H.; Kim, M.; Nasir, N.; Suleman, M.; Lee, S.; Seo, Y. Oxidation-Driven Auto-Conversion of $Ti_3C_2T_x$ MXene to TiO_2 Nanoparticles for Photocatalytic Applications. *J. Alloys Compd.* **2024**, *976*, No. 173399.
(34) Alsaffar, F.; Alodan, S.; Alrasheed, A.; Alhussain, A.; Alrubaiq, N.; Abbas, A.; Amer, M. R. Raman Sensitive Degradation and Etching Dynamics of Exfoliated Black Phosphorus. *Sci. Rep.* **2017**, *7* (1), No. 44540.
(35) Shimizu, M.; Koya, T.; Nakahigashi, A.; Urakami, N.; Yamakami, T.; Arai, S. Kinetics Study and Degradation Analysis through Raman Spectroscopy of Graphite as a Negative-Electrode Material for Potassium-Ion Batteries. *J. Phys. Chem. C* **2020**, *124* (24), 13008−13016.
(36) Lin, Z.; Guo, X.; He, Z.; Liang, X.; Wang, M.; Jin, G. Thermal Degradation Kinetics Study of Molten Polylactide Based on Raman Spectroscopy. *Polym. Eng. Sci.* **2021**, *61* (1), 201−210.
(37) Mikulics, M.; Adam, R.; Sobolewski, R.; Heidtfeld, S.; Cao, D.; Bürgler, D. E.; Schneider, C. M.; Mayer, J.; Hardtdegen, H. H. Nano-LED Driven Phase Change Evolution of Layered Chalcogenides for Raman Spectroscopy Investigations. *FlatChem* **2022**, *36*, No. 100447.
(38) Xue, W.; Yan, H.; He, Y.; Wu, L.; Zhang, X.; Wu, Y.; Xu, J.; He, J.; Yan, C.; Meng, H. Identifying the Molecular Origins of Green BN-TADF Material Degradation and Device Stability via in Situ Raman Spectroscopy. *Chem. - Eur. J.* **2022**, *28* (36), No. e202201006.
(39) Mikulics, M.; Adam, R.; Chen, G.; Chakraborty, D.; Cheng, J.; Pericolo, A.; Komissarov, I.; Bürgler, D. E.; Heidtfeld, S. F.; Serafini, J.; et al. Determination of Thermal Damage Threshold in THz Photomixers Using Raman Spectroscopy. *Crystals* **2023**, *13* (8), No. 1267.
(40) Naqvi, F. H.; Ko, J.-H. Structural Phase Transitions and Thermal Degradation Process of $MAPbCl_3$ Single Crystals Studied by Raman and Brillouin Scattering. *Materials* **2022**, *15* (22), No. 8151.
(41) Hu, T.; Hu, M.; Gao, B.; Li, W.; Wang, X. Screening Surface Structure of MXenes by High-Throughput Computation and Vibrational Spectroscopic Confirmation. *J. Phys. Chem. C* **2018**, *122* (32), 18501−18509.
(42) Sarycheva, A.; Gogotsi, Y. Raman Spectroscopy Analysis of the Structure and Surface Chemistry of $Ti_3C_2T_x$ MXene. *Chem. Mater.* **2020**, *32* (8), 3480−3488.
(43) Benchakar, M.; Loupias, L.; Garnero, C.; Bilyk, T.; Morais, C.; Canaff, C.; Guignard, N.; Morisset, S.; Pazniak, H.; Hurand, S.; Chartier, P.; Pacaud, J.; Mauchamp, V.; Barsoum, M. W.; Habrioux, A.; Célérier, S. One MAX Phase, Different MXenes: A Guideline to Understand the Crucial Role of Etching Conditions on $Ti_3C_2T_x$ Surface Chemistry. *Appl. Surf. Sci.* **2020**, *530*, No. 147209.
(44) Naguib, M.; Mashtalir, O.; Lukatskaya, M. R.; Dyatkin, B.; Zhang, C.; Presser, V.; Gogotsi, Y.; Barsoum, M. W. One-Step Synthesis of Nanocrystalline Transition Metal Oxides on Thin Sheets of Disordered Graphitic Carbon by Oxidation of MXenes. *Chem. Commun.* **2014**, *50* (56), 7420−7423.
(45) Salles, P.; Pinto, D.; Hantanasirisakul, K.; Maleski, K.; Shuck, C. E.; Gogotsi, Y. Electrochromic Effect in Titanium Carbide MXene Thin Films Produced by Dip-Coating. *Adv. Funct. Mater.* **2019**, *29* (17), No. 1809223.
(46) Lorencova, L.; Bertok, T.; Dosekova, E.; Holazova, A.; Paprckova, D.; Vikartovska, A.; Sasinkova, V.; Filip, J.; Kasak, P.; Jerigova, M.; Velic, D.; Mahmoud, K. A.; Tkac, J. Electrochemical Performance of $Ti_3C_2T_x$ MXene in Aqueous Media: Towards Ultrasensitive H_2O_2 Sensing. *Electrochim. Acta* **2017**, *235*, 471−479.
(47) Lipatov, A.; Alhabeb, M.; Lukatskaya, M. R.; Boson, A.; Gogotsi, Y.; Sinitskii, A. Effect of Synthesis on Quality, Electronic

https://doi.org/10.1021/acsnano.4c02150
ACS Nano 2024, 18, 13184−13195

Properties and Environmental Stability of Individual Monolayer Ti_3C_2 MXene Flakes. *Adv. Electron. Mater.* **2016**, *2* (12), No. 1600255.
(48) Gonçalves, M.; Melikyan, A.; Minassian, H.; Makaryan, T.; Petrosyan, P.; Sargsian, T. Interband, Surface Plasmon and Fano Resonances in Titanium Carbide (MXene) Nanoparticles in the Visible to Infrared Range. *Photonics* **2021**, *8* (2), No. 36.
(49) Hu, T.; Wang, J.; Zhang, H.; Li, Z.; Hu, M.; Wang, X. Vibrational Properties of Ti_3C_2 and $Ti_3C_2T_2$ (T = O, F, OH) Monosheets by First-Principles Calculations: A Comparative Study. *Phys. Chem. Chem. Phys.* **2015**, *17* (15), 9997−10003.
(50) Björk, J.; Rosen, J. Functionalizing MXenes by Tailoring Surface Terminations in Different Chemical Environments. *Chem. Mater.* **2021**, *33* (23), 9108−9118.
(51) Berger, E.; Lv, Z.-P.; Komsa, H.-P. Raman Spectra of 2D Titanium Carbide MXene from Machine-Learning Force Field Molecular Dynamics. *J. Mater. Chem. C* **2023**, *11* (4), 1311−1319.
(52) Ibragimova, R.; Erhart, P.; Rinke, P.; Komsa, H.-P. Surface Functionalization of 2D MXenes: Trends in Distribution, Composition, and Electronic Properties. *J. Phys. Chem. Lett.* **2021**, *12* (9), 2377−2384.
(53) Wang, H.-W.; Naguib, M.; Page, K.; Wesolowski, D. J.; Gogotsi, Y. Resolving the Structure of $Ti_3C_2T_x$ MXenes through Multilevel Structural Modeling of the Atomic Pair Distribution Function. *Chem. Mater.* **2016**, *28* (1), 349−359.
(54) Bashir, T.; Ismail, S. A.; Wang, J.; Zhu, W.; Zhao, J.; Gao, L. MXene Terminating Groups O, −F or −OH, −F or O, −OH, −F, or O, −OH, −Cl? *J. Energy Chem.* **2023**, *76*, 90−104.
(55) Shi, C.; Beidaghi, M.; Naguib, M.; Mashtalir, O.; Gogotsi, Y.; Billinge, S. J. L. Structure of Nanocrystalline Ti_3C_2 MXene Using Atomic Pair Distribution Function. *Phys. Rev. Lett.* **2014**, *112* (12), No. 125501.
(56) Zhang, Z.; Yao, Z.; Zhang, X.; Jiang, Z. 2D Carbide MXene under Postetch Low-Temperature Annealing for High−Performance Supercapacitor Electrode. *Electrochim. Acta* **2020**, *359*, No. 136960.
(57) Han, M.; Yin, X.; Wu, H.; Hou, Z.; Song, C.; Li, X.; Zhang, L.; Cheng, L. Ti_3C_2 MXenes with Modified Surface for High-Performance Electromagnetic Absorption and Shielding in the X-Band. *ACS Appl. Mater. Interfaces* **2016**, *8* (32), 21011−21019.
(58) Halim, J.; Persson, I.; Eklund, P.; Persson, P. O. Å.; Rosen, J. Sodium Hydroxide and Vacuum Annealing Modifications of the Surface Terminations of a Ti_3C_2 (MXene) Epitaxial Thin Film. *RSC Adv.* **2018**, *8* (64), 36785−36790.
(59) Hart, J. L.; Hantanasirisakul, K.; Lang, A. C.; Anasori, B.; Pinto, D.; Pivak, Y.; van Omme, J. T.; May, S. J.; Gogotsi, Y.; Taheri, M. L. Control of MXenes' Electronic Properties through Termination and Intercalation. *Nat. Commun.* **2019**, *10* (1), No. 522.
(60) Alhabeb, M.; Maleski, K.; Anasori, B.; Lelyukh, P.; Clark, L.; Sin, S.; Gogotsi, Y. Guidelines for Synthesis and Processing of Two-Dimensional Titanium Carbide ($Ti_3C_2T_x$ MXene). *Chem. Mater.* **2017**, *29* (18), 7633−7644.
(61) Dillon, A. D.; Ghidiu, M. J.; Krick, A. L.; Griggs, J.; May, S. J.; Gogotsi, Y.; Barsoum, M. W.; Fafarman, A. T. Highly Conductive Optical Quality Solution-Processed Films of 2D Titanium Carbide. *Adv. Funct Mater.* **2016**, *26* (23), 4162−4168.
(62) Kang, Z.; Ma, Y.; Tan, X.; Zhu, M.; Zheng, Z.; Liu, N.; Li, L.; Zou, Z.; Jiang, X.; Zhai, T.; Gao, Y. MXene−Silicon Van Der Waals Heterostructures for High-Speed Self-Driven Photodetectors. *Adv. Electron. Mater.* **2017**, *3* (9), No. 1700165.
(63) Mauchamp, V.; Bugnet, M.; Bellido, E. P.; Botton, G. A.; Moreau, P.; Magne, D.; Naguib, M.; Cabioc'h, T.; Barsoum, M. W. Enhanced and Tunable Surface Plasmons in Two-Dimensional Ti_3C_2 Stacks: Electronic Structure versus Boundary Effects. *Phys. Rev. B* **2014**, *89* (23), No. 235428.
(64) Kiefer, W. *Surface Enhanced Raman Spectroscopy: Analytical, Biophysical and Life Science Applications*; John Wiley & Sons, 2011.
(65) Le Ru, E.; Etchegoin, P. *Principles of Surface-Enhanced Raman Spectroscopy: And Related Plasmonic Effects*; Elsevier, 2008.
(66) Xia, F.; Lao, J.; Yu, R.; Sang, X.; Luo, J.; Li, Y.; Wu, J. Ambient Oxidation of Ti_3C_2 MXene Initialized by Atomic Defects. *Nanoscale* **2019**, *11* (48), 23330−23337.
(67) Kumar, S.; Park, H. M.; Singh, T.; Kumar, M.; Seo, Y. Long-Term Stability Studies and Applications of $Ti_3C_2T_x$ MXene. *Int. J. Energy Res.* **2023**, *2023*, No. 5275439.
(68) Lotfi, R.; Naguib, M.; Yilmaz, D. E.; Nanda, J.; van Duin, A. C. T. A Comparative Study on the Oxidation of Two-Dimensional Ti_3C_2 MXene Structures in Different Environments. *J. Mater. Chem. A* **2018**, *6* (26), 12733−12743.
(69) Smith, M. W.; Dallmeyer, I.; Johnson, T. J.; Brauer, C. S.; McEwen, J. S.; Espinal, J. F.; Garcia-Perez, M. Structural Analysis of Char by Raman Spectroscopy: Improving Band Assignments through Computational Calculations from First Principles. *Carbon* **2016**, *100*, 678−692.
(70) Childres, I.; Jauregui, L. A.; Park, W.; Cao, H.; Chen, Y. P. Raman Spectroscopy of Graphene and Related Materials. In *New Developments in Photon and Materials Research*; Citeseer, 2013; Vol. *1*, pp 1−20.
(71) Ma, J.; Li, W.; Morgan, B. J.; Światowska, J.; Baddour-Hadjean, R.; Body, M.; Legein, C.; Borkiewicz, O. J.; Leclerc, S.; Groult, H.; Lantelme, F.; Laberty-Robert, C.; Dambournet, D. Lithium Intercalation in Anatase Titanium Vacancies and the Role of Local Anionic Environment. *Chem. Mater.* **2018**, *30* (9), 3078−3089.
(72) Hou, C.; Xie, J.; Yang, H.; Chen, S.; Liu, H. Preparation of Cu_2O@$TiOF_2$/TiO_2 and Its Photocatalytic Degradation of Tetracycline Hydrochloride Wastewater. *RSC Adv.* **2019**, *9* (65), 37911−37918.
(73) Liu, S.; Yu, J.; Wang, W. Effects of Annealing on the Microstructures and Photoactivity of Fluorinated N-Doped TiO_2. *Phys. Chem. Chem. Phys.* **2010**, *12* (38), 12308−12315.
(74) Louvain, N.; Karkar, Z.; El-Ghozzi, M.; Bonnet, P.; Guérin, K.; Willmann, P. Fluorination of Anatase TiO_2 towards Titanium Oxyfluoride $TiOF_2$: A Novel Synthesis Approach and Proof of the Li-Insertion Mechanism. *J. Mater. Chem. A* **2014**, *2* (37), 15308−15315.

https://doi.org/10.1021/acsnano.4c02150
ACS Nano 2024, 18, 13184−13195